6. Martian Geomorphologic Effects on Propagation

6.1 Introduction

Mars has very complicated geomorphologic (or physiographic) features. These ground structures will affect the radio wave propagation, especially for low-elevation angle propagation. The surface features will affect wave propagation in the following ways [Carr, 1981; CCIR, 1986a and b; Simpson et al., 1992; Goldhirsh and Vogel, 1998]:

1. Multipath at low elevation angle due to reflection and diffraction by terrain and rocks [Vogel and Goldhirsh, 1988]; the ray can arrive at the receiver through more than one path, causing signal fading and attenuation. These features will affect land mobile telecommunication on Mars.

2. Surface reflection, surface roughness, tilt angle, albedo, reflectivity, etc.

3. Atmospheric and climate features associated with surface physiographic structures: fog, water clouds, and dust storms in certain regions.

Reflected radio wave intensities at the Martian surface are strongly dependent on the surface material composition and roughness. There are some changes in the dispersion, polarization, shape, and strength of radio signal echoes due to surface absorption and scattering. In turn, we can use these features to study Martian surface structures. They include surface roughness, reflectivity, small-scale structure size, etc. Surface material properties (reflectivity or dielectric constant) may be inferred from signal changes. For a smooth interface and a normal incident wave, the reflection coefficient, R, is simply related to the dielectric constant ε by

$$R = \left[\frac{1 - \sqrt{\varepsilon}}{1 + \sqrt{\varepsilon}} \right] \tag{6-1}$$

where ε can have an imaginary part, which is responsible for loss and absorption. In general, lower material densities have lower reflectivity for a given composition. For example, a solid rock has $\varepsilon \sim 5$ to 9 ($|R| \sim 0.15$ to 0.25), while typical soils are in the range $\varepsilon \sim 2$ to 3 ($|R| \sim 0.03$ to 0.07). The Martian surface has a diverse structure; depending on location, rms surface tilt angles have been found to vary over the range 0.25° to 10°, while reflectivity covers at least 0.03 to 0.25 [Simpson et al., 1992; Bedrossian et al., 2002].

The geomorphology of Mars has an obvious north-south asymmetry. Much of southern hemisphere is heavily cratered. The density of craters larger than 20 km in diameter is particularly high. In contrast, most of the northern hemisphere is covered by plains that have much smaller crater densities, as shown in Figure 6-1 [Wu, 1978; Carr, 1981; Smith et al., 1998]. Among the most impressive features of the planet are the large volcanoes [Mouginis-Mark et al., 1992]. The three largest volcanoes lie in the Tharsis bulge region (centered on the equator at about 115° W). The tallest one, Olympus Mons, is more than 700 km across, with a summit 25 km above the surrounding plains. All Tharsis volcanoes are enormous by terrestrial standards, at 27 km above the Mars reference surface, which is defined as an atmospheric pressure 6.1 mb level [Malin et al., 1998].

Vast dune fields, various albedo patterns that change with time, wind-eroded hills, and drifts of fine-grained material observed at two Viking Lander and Mars Pathfinder sites are all attributed to aeolian processes. Sand dunes are observed in all region of Mars. The largest area of dunes occurs in a broad belt that partly surrounds the north polar ice cap between 75° and 80° N [Carr, 1981]. The only three sites on Mars viewed close up show surfaces sprinkled with rocks in the centimeter to meter size range. In some areas, bedrock can occasionally be seen [Simpson et al., 1992]. At the Mars Pathfinder site shown in Figure 6-2, the images revealed a rocky plain (about 20 percent covered by rocks) that appears to have been deposited and shaped by catastrophic floods. Large rocks are flat-topped and often perched. Between the rocks are mostly fine-grained (< 100 μm) materials. Soils vary from the bright-red dust to darker-gray material. Their composition is mainly sulfur, iron, magnesium, and silicon [Malin et al., 1998].

There is evidence that in the past a denser Martian atmosphere may have allowed water to flow on the planet. Physical features closely resembling shorelines, gorges, riverbeds, and islands suggest that great rivers once marked the planet. Large channels can also be seen everywhere on the Martian surface [Baker et al., 1992]. Some of these channels are several hundred kilometers long and tens of kilometers across. They show numerous indications of early fluvial activity.

A recent landmark discovery is that MGS imagery shows many gullies that may have been be caused by current sources of liquid water at or near the surface of Mars [Malin and Edgett, 2000]. These gullies appear so fresh that they might have been formed yesterday. Figure 6-3 shows an image made by the MGS camera. The gullies observed on cliffs, usually in crater or valley walls, are made up of a deep channel with a collapsed region at its upper end. Nearly all gullies occur between latitudes 30° and 70°. The lack of small craters superimposed on the channels and apron deposits indicates that these features are geologically young. It is possible that these gullies indicate that liquid water is present below the surface of Mars today. This suggests that Mars may have a significant amount of underground water. The atmospheric pressure at the Martian surface is about 6.1 mb (more than 100 times less than it is at sea level on Earth). Liquid water would immediately begin to boil if it were exposed at the Martian surface. At the downstream end of the gully, water may be quickly evaporated or may flow back underground [Malin and Edgett, 2000].

However, the two most significant geomorphological features on Mars are its polar ice caps and its “grand canyon” system. Some layered deposits lie on both polar regions and also extend outward about 10° in latitude [Thomas et al., 1992]. They consist of water or CO_2 ice. On the east side of Tharsis, and just south of the equator, there is a vast interconnected canyon system. In most places, the canyons are more than 3 km deep and 100 km across. This canyon system is called Valles Marineris [Lucchitta et al., 1992]. These features are distinctively different from the rest of the planet. We describe the effects of the geomorphologic features on radio wave propagation in the following paragraphs.

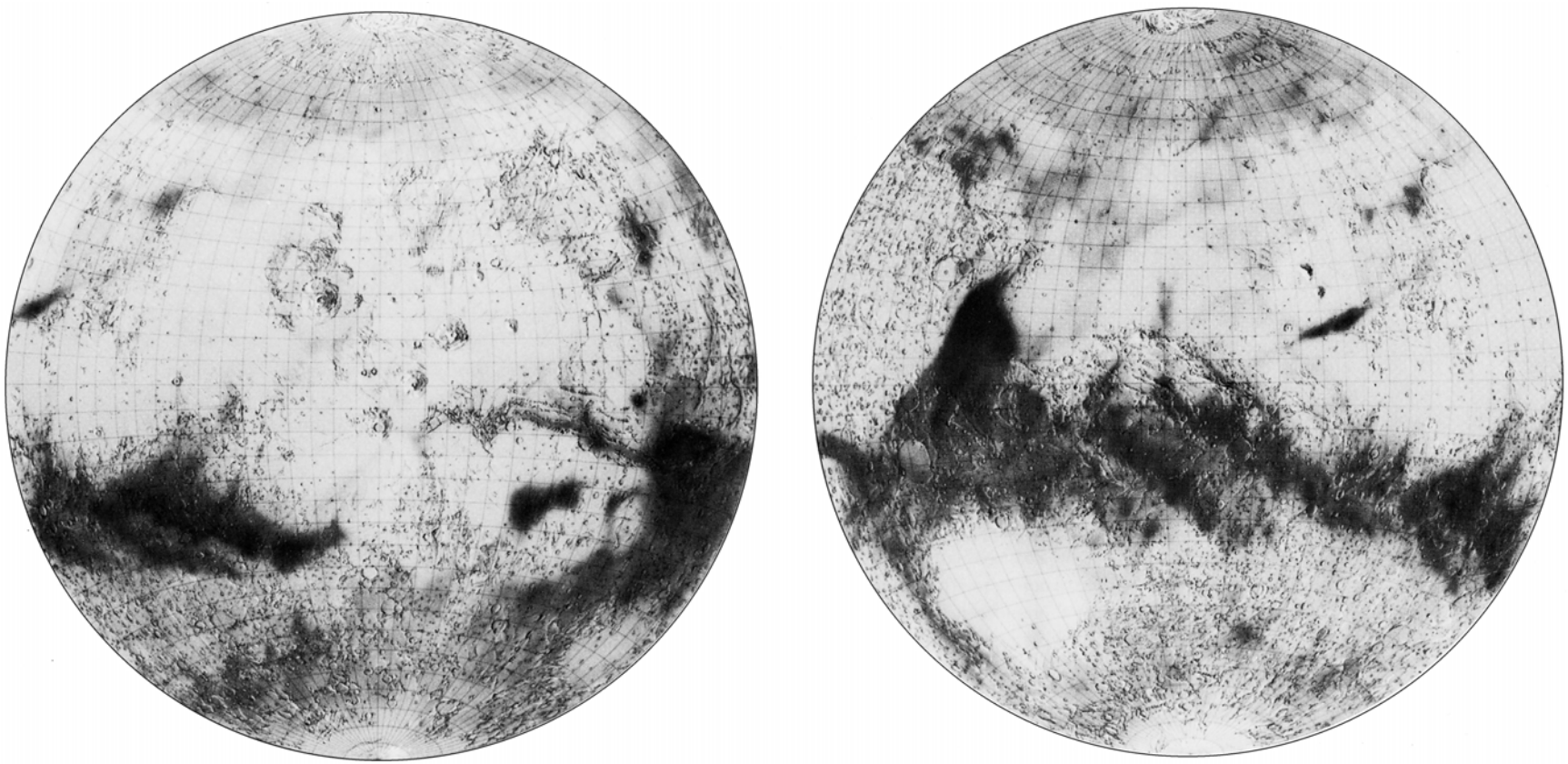

Figure 6-1. Two Lambert Maps Show the Martian Surface Features. The left figure is centered at 120° W; the right at 240° W. There is an obvious north-south asymmetry in the physiography.

Figure 6-2. Image of Mars Mosaic Showing the Mars Pathfinder Landing Area. The large, prominent rocks comprise the "Rock Garden" which is similar to those of depositional plains in terrestrial catastrophic floods.

Figure 6-3. Image Taken by NASA's Mars Global Surveyor Showing Signs of Water Erosion and Debris Flow. Gullies erode into the wall of a meteor impact crater in Noachis Terra on Mars. Channels and associated aprons of debris are interpreted to have formed by ground water seepage, surface runoff, and debris flow. The scene covers an area approximately 3 km (about 2 miles) wide by 6.7 km (4.1 miles) high, located near 54.8 degrees South by 342.5 degrees West.

6.2 Mars Polar Ice Caps

The Martian polar caps are the first features to be recognized from Earth. Three hundred years ago, Giovanni Cassini (1625–1712) found that both white polar caps changed their sizes with the Martian seasons. We know that Earth's two polar regions (the Arctic and the Antarctic) have huge ice sheets. Ice sheets retreat and advance with the seasons. Similarly, Mars also has ice caps at its polar regions. However, their sizes are much smaller, only 4% of the size of the Earth's Antarctic ice sheet. The Martian polar ice cap also retreats from its maximum (2000 km across) to 300 km (residual cap) in summer, as shown in Figure 6-4 [Thomas et al., 1992].

Both polar ice caps consist of seasonal caps and residual caps. Seasonal caps advance and recede with seasons. During southern winter, Mars is close to aphelion and its orbit moves relatively slowly. Thus, southern winters are colder and longer than northern winters. In contrast, southern summers occur close to the Martian perihelion, so they are relatively hot and short. Only a small remnant cap is left. At its smallest the southern cap is about 350 km across, compared with 1,000 km for the remnant northern cap.

The formation of the caps is not observed because, during the fall, clouds of CO_2 form over the polar hood regions as the CO_2 condenses into the caps. At their maximum extent, the polar caps are roughly circular around the pole. While the southern cap edge can touch the 60° S latitude, the northern one extends to about 65° N. The retreat of the polar caps is nonuniform in longitude but similar from year to year. As the seasonal cap contracts, the characteristic "swirl" texture of the permanent cap emerges. The pattern is caused by preferential removal of frost on equatorward-facing slopes in valleys. The slopes have a roughly spiral pattern in a clockwise direction [Zuber et al., 1998].

The northern residual cap is almost certainly water ice. Brightness temperatures over most of the cap are near 205 K, close to the frost point of water at Martian atmospheric pressure. Solid CO_2 is unlikely to be present in large amounts at this temperature. The southern residual ice cap has a temperature around 160 K, much colder than the northern cap at the same season. This temperature is close to the CO_2 frost point, and thus, the southern cap should predominantly consist of CO_2 ice.

To explain this difference, Pollack et al. [1979] suggested that dust storms started during southern hemispheric summer could play an important role in the residual caps. During that time, the northern cap is formed through CO_2 condensation. Dust in the atmosphere can be seeds for ice condensation, and this would remove a large percentage of the dust grains from the Martian atmosphere. When the southern polar cap is forming (southern winter), there is little dust in the air. Thus, the south polar cap has clean, high-albedo ice that absorbs relatively less solar radiation and is also partly shielded by dust clouds from Sun light. In contrast, the northern cap has "dirty" ice, over which the atmosphere is clear during the southern hemispheric summer. This results in warmer temperatures on the remnant northern summer cap (complete vaporization of CO_2) than on the southern cap (retention of small amounts of CO_2 ice) [Thomas et al., 1992].

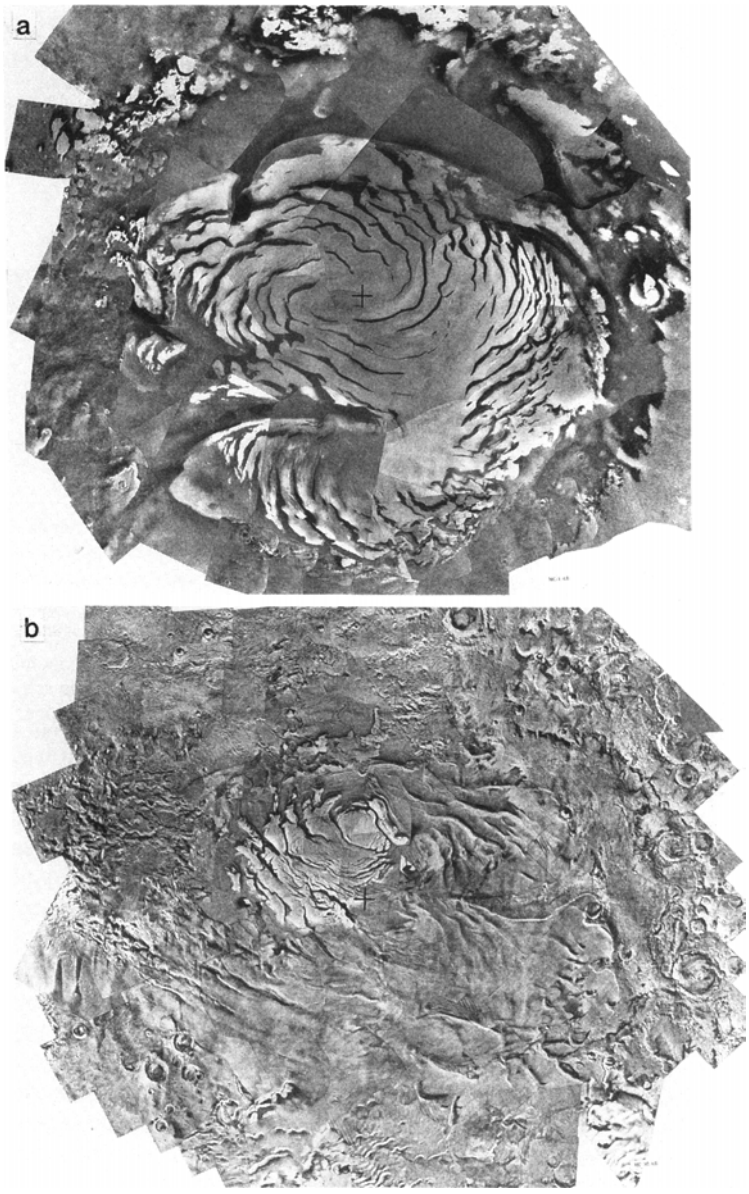

Figure 6-4. Mosaics of Viking Orbiter Images of Polar Regions in the Southern Summer. (a) North polar region; (b) South polar region (from Thomas et al., 1992).

The laser altimeter aboard Mars Global Surveyor produced the first three-dimensional views of the Mars' northern polar cap. This view is shown in Figure 6-5 [Isbell et al., 1998]. During the spring and summer of 1998, as the spacecraft orbited Mars, the altimeter sent laser pulses toward the planet. Very precise elevation data were obtained (1 km spatial resolution, 5–30 m vertical accuracy). Topographic measurements by MGS revealed that the ice cap is about 1200 km across, with a maximum thickness of 3 km. At some sites, the cap is cut by canyons and troughs that plunge to as deep as 1 km beneath the surface. However, some areas are extremely smooth, with only a few meters of changes over many kilometers. It is estimated that the polar cap has a volume of 1.2 million km^3 of water ice. For comparison, this is less than half that of the Earth's Greenland ice cap [Zuber et al., 1998].

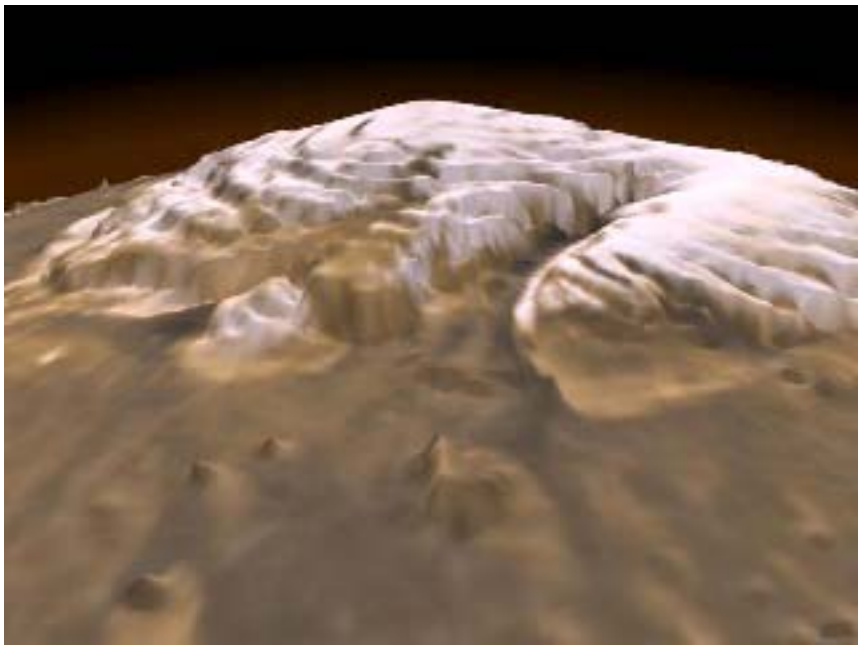

Figure 6-5. Three-Dimensional View of the North Polar Region of Mars from MGS Orbiter Laser Altimeter. The ice cap has a maximum thickness of about 3 km [Isbell et al., 1998; Zuber et al., 1998].

Figure 6-6 shows how diffraction and multipath affect radio wave propagation between a Mars-orbiting satellite and a lander within a polar cap ice trough [CCIR, 1986a and b; Goldhirsh and Vogel, 1998]. As shown in this cartoon, a rover is inside an ice trough, which is about 2 km high and 4 km wide. When the orbiter is at time t_1, even though it cannot directly see the rover, the signals transmitted from the satellite can still reach the rover by a diffracted ray R_1, through the trough edge point T, and a reflected ray $R_1^{'}$ through a reflection from another ice wall. Diffraction is an important possible means of communication between the rover and a satellite beyond the line of sight. On the basis of Huygen's principle, every elementary area of a wavefront can be regarded as a source of secondary spherical waves. Thus, at point T the signal coming from the satellite is a new wave source to propagate to the rover. At times t_2 and t_3, the satellite can directly link to the rover through the rays R_2 and R_3. At the same time, there also are two reflected rays, $R_2^{'}$ and $R_3^{'}$, that arrive at the rover. These reflected rays are delayed in time and phase relative to the direct rays. Assuming that the height of point T on the right ice wall is h_1 (about 2.0 km), the elevation angle of the right side edge relative to the rover is α, while the satellite's elevation angle is θ at time t_1 beyond the line of sight. Also, assuming that the directly received signals R_2 or R_3 (at t_2 or t_3 respectively) at the rover have an intensity E_0,

$$E_{R_2} = E_{R_3} = E_0 \tag{6-2}$$

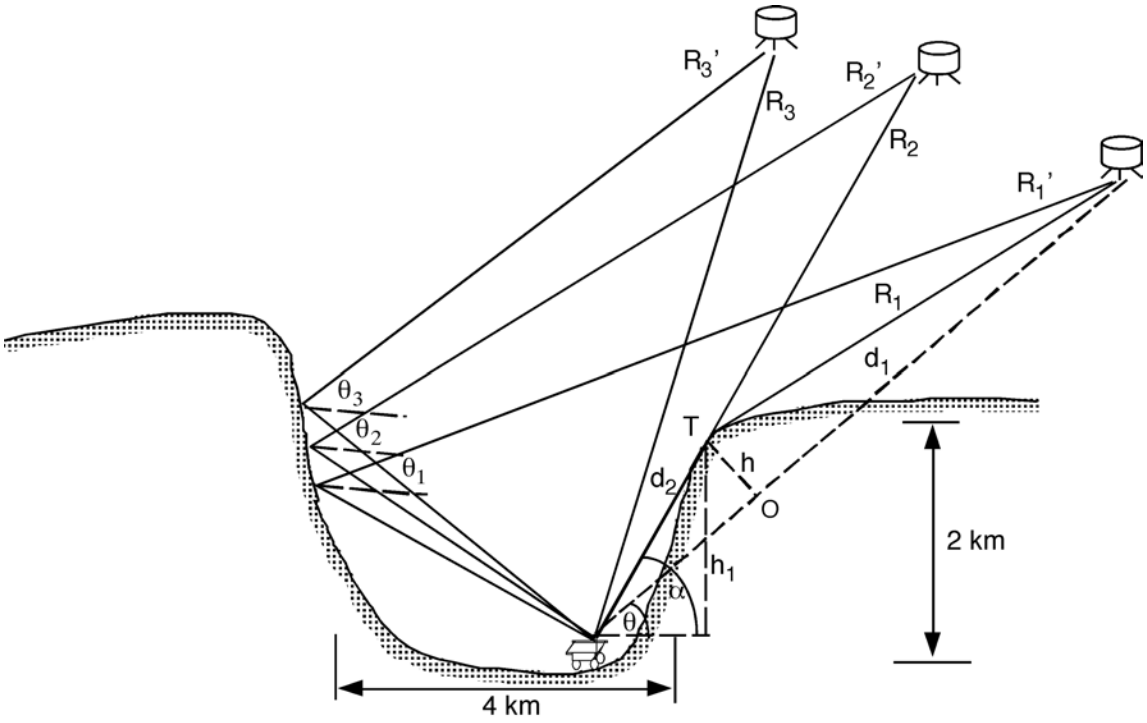

Figure 6-6. Graphic Diagram Showing Radio Ray Paths Between a Rover Within a Canyon and a Satellite Orbiting Mars. Below the line of sight, through ray diffraction and reflection, the rover may still communicate with the satellite, but radio signals will have a higher attenuation than the direct link.

The diffracted signal has an intensity (instead of strength) of

$$10\log_{10}\frac{E_{R_1}}{E_0} = -J(\nu) \tag{6-3}$$

$$E_{R_1} = E_0 10^{-J(\nu)/10} \tag{6-4}$$

where

$$J(\nu) = 6.9 + 20\log(\sqrt{(\nu-0.1)^2+1}+\nu-0.1) \tag{6-5}$$

is diffraction loss (in dB), and the parameter ν is

$$v = h\sqrt{\frac{2}{\lambda}(\frac{d}{d_1 d_2})} \tag{6-6}$$

This comes from the attenuation over a single knife-edge obstacle [Deygout, 1966]. In Equation (6-6), $h = \frac{sin(\alpha - \theta)}{sin\alpha} h_1$, λ is the signal wavelength, d_1 and d_2 are distances of two ends of the path from the top of the obstacle, and d is total path length. Because $J(\nu)$ is usually greater than 6.9, the diffracted signal intensity over a canyon edge, E_{R_1}, is less than $0.2E_0$.

The reflected signals along the paths $R_1^{'}$, $R_2^{'}$, and $R_3^{'}$, have intensities

$$E_{1,2,3}^{'} = \rho E_0 e^{i\phi_2} = (|\ \rho\ | e^{i\phi_1})(|\ E_0\ | e^{i\phi_2}) = |\ \rho\ ||\ E_0\ | e^{i\Phi} \tag{6-7}$$

where ρ is reflection coefficient, which may be a complex and will not have a magnitude of unity. ϕ_1 is the phase of reflection coefficient, and ϕ_2 is the phase shift corresponding to the path length difference (Δl) between the reflected ray and the direct ray. Thus, the phase angle Φ of the reflected ray relative to the diffracted ray is

$$\Phi = \phi_1 + \phi_2 = \phi_1 + \frac{2\pi\Delta l}{\lambda} \tag{6-8}$$

The signal intensities received by the rover should be a combination of the direct ray (or diffracted ray) E_R and the reflected ray E' [Beckmann and Spizzichino, 1963]. At t_2 and t_3

$$E_{2,3} = E_0 + E_{2,3}^{'} = |\ E_0\ | \sqrt{1 + |\ \rho\ |^2 - 2\ |\ \rho\ | \cos\Phi} \tag{6-9}$$

At t_1, total field is

$$E_1 = E_{R_1} + E_1^{'} = |\ E_0\ | \sqrt{10^{-2J(\nu)/10} + |\ \rho\ |^2 - 2\ |\ \rho\ | 10^{-J(\nu)/10} \cos\Phi} \tag{6-10}$$

Except for direct measurements, it is almost impossible to calculate a precise value for Φ, even though we know all the geometric parameters, because the path-length difference depends largely on atmospheric effects on the ray paths (curved to some degrees and variable with time).

When $\rho = 1$, we have

$$E_{2,3} = 2\ |\ E_0\ | \cdot sin\frac{\Phi}{2} \tag{6-11}$$

We have maximum and minimum intensities for $E_{2,3}$ of

$$E_{\max} = |\ E_0\ | (1 + |\ \rho\ |) \quad \text{when } \Phi = \pi \tag{6–12}$$

$$E_{\min} = |\ E_0\ | (1 - |\ \rho\ |) \quad \text{when } \Phi = 0 \tag{6–13}$$

For E_1, we have

$$E_{\max} = (|\rho| + 10^{-J(\nu)/10}) |E_0| \quad \text{when } \Phi = \pi \tag{6–14}$$

$$E_{\min} = (|\rho| - 10^{-J(\nu)/10}) |E_0| \quad \text{when } \Phi = 0 \tag{6–15}$$

Its intensity depends on both of reflection coefficient and diffraction attenuation.

6.3 Mars "Grand Canyon" Valles Marineris

Just south of the equator, between the longitudes 30° W and 110° W, are several enormous, interconnected canyons, which have been collectively called Valles Marineris. The Valles Marineris is the most spectacular geologic feature on Mars. The canyon is 4000 km long, 150 km wide, and 10 km deep as shown in Figure 6-7. By comparison, the Grand Canyon is 450 km long, 30 km across, at its widest point, and 2 km deep. Most of the interconnected canyons lack indications of fluvial action on their floors. They appear to result from faulting along east-west faults. The canyons are widest and deepest in the central section, between 65° W and 77° W, where three huge parallel troughs are each close to 200 km across [Lucchitta et al., 1992].

Canyon walls usually have steep gradients and stand at great heights relative to their top plateaus. Many canyon walls have slope angles greater than 35°, their limit of mechanical stability. Some walls have two parts, upper parts with steep slopes and lower parts with sharp-crested ridges, which are oriented perpendicular to the canyons. The canyon floors vary considerably from place to place. Where the canyons are narrow, the floors tend to be segmented. Where the troughs are wide, the floors are flatter and better integrated and may include landslide deposits.

Figure 6-8 shows laser altimeter reflectivity measurements from Mars taken by MGS during fall 1997 (L_s = 198-212). The small reflectivity values over the Valles Marineris canyon can be interpreted as a combination of surface geometric albedo and two-way atmospheric transmission [Ivanov and Muhleman, 1998]. The reflectivity (R) is the ratio of returned laser energy to the emitted laser energy. R is affected by the surface albedo (A) of the underlying terrain and extinction of the photons from the laser beam by atmospheric aerosols. R can be expressed as

$$R = A \; e^{-2\tau} \tag{6-16}$$

where τ is the atmospheric opacity of the atmosphere. Using relative surface albedo data from Viking [Colburn et al., 1989], large atmospheric opacity values are obtained, which are interpreted in terms of atmospheric aerosol loading in the canyons. There are large opacity changes with depth within a canyon.

NASA is planning a series of Mars Micromissions for 2003, 2005, and later. One of the possible missions, called Mars Airborne Geophysical Explorer (MAGE), will use an airplane to determine how the canyons of Valles Marineris formed and have subsequently evolved. The planned Mars airplane, known as "Kitty Hawk," will carry a payload of several instruments on a 3-hour,

1800-km flight over the canyon. Fully deployed, the 135-kg airplane has a long (9.75 m) wingspan and a comparatively small body (because of lower Martian pressure), as shown in Figure 6-9. Using the airplane, a wide range of gravitational and topographic features can be closely surveyed. The low-drag design will allow Kitty Hawk to fly at a constant pressure altitude, which will vary from 1 km to 9 km from the canyon rim to its floor. To drive the rear-mounted propeller and provide electric power, the aircraft will use a hydrazine-fueled engine. Possibly in 2010, cruise and relay vehicle (CARV) will carry a Mars atmosphere entry vehicle housing the Kitty Hawk airplane from Earth to Mars. After releasing the entry vehicle at Mars, CARV will act as a data relay to collect data from the airplane and relay it to Earth.

Figure 6-10 shows an example of how diffraction over a canyon edge affects communication between the satellite and a Martian airplane [CCIR, 1986a]. Because of the roughness of the rock surface, no multipath (like those in Figure 6-5) caused by reflection from walls is considered in this calculation. A Martian airplane is inside the canyon, flying along the 6.1-mb pressure level. The altitude difference between the airplane and the canyon edge is h_1 (about 1.0 km). The elevation angle of the canyon edge relative to the airplane is α, while the satellite's elevation angle is θ at time t_1 behind the sight. The radio wave R_1 will be diffracted by the canyon edge at point T. Assuming that directly received signals R_2 or R_3 (respectively at t_2 or t_3) by the airplane have an intensity E_0, the diffracted signal will have an intensity

$$E_{R_1} = E_0 10^{-J(\nu)/10} \tag{6-17}$$

where $J(\nu)$, ν, has the same definitions as shown in Equation (6-4). Parameters h_1, d_1, d_2, d, θ, and α are also defined as in Figure 6-10.

6.4 Summary and Recommendations

Mars has very complicated surface geomorphologic structures. These structures will affect radio wave propagation from surface equipment and from an aircraft to a satellite when the satellite is at low elevation angles. When terrain or rocks block the direct radio wave rays, a lander can sometimes still communicate with a satellite through diffracted and/or reflected rays. The intensities of diffracted wave signals are reduced by at least a factor of 5 relative to direct signals. Reflected signal intensity depends largely on the reflection coefficient of the reflecting materials. Multipath can also cause signal amplitude fading and attenuation due to phase shifts. Sometimes, when reflected signals have a nearly 180° phase difference from direct (or diffracted) signals, the combined signal intensity can be severely attenuated (by ~–30 dB). This will be a potential problem for future Mars communication with mobile land sources and with colonies. Multipath fading effects can be modeled by a Rayleigh or Ricean model. Fading mechanisms and distributions of Martian rocks and terrain in various spatial scales need to be studied in the future. Currently we have very limited information about the surface and rock properties. We recommend inclusion of such measurements and experiments in future Mars missions.

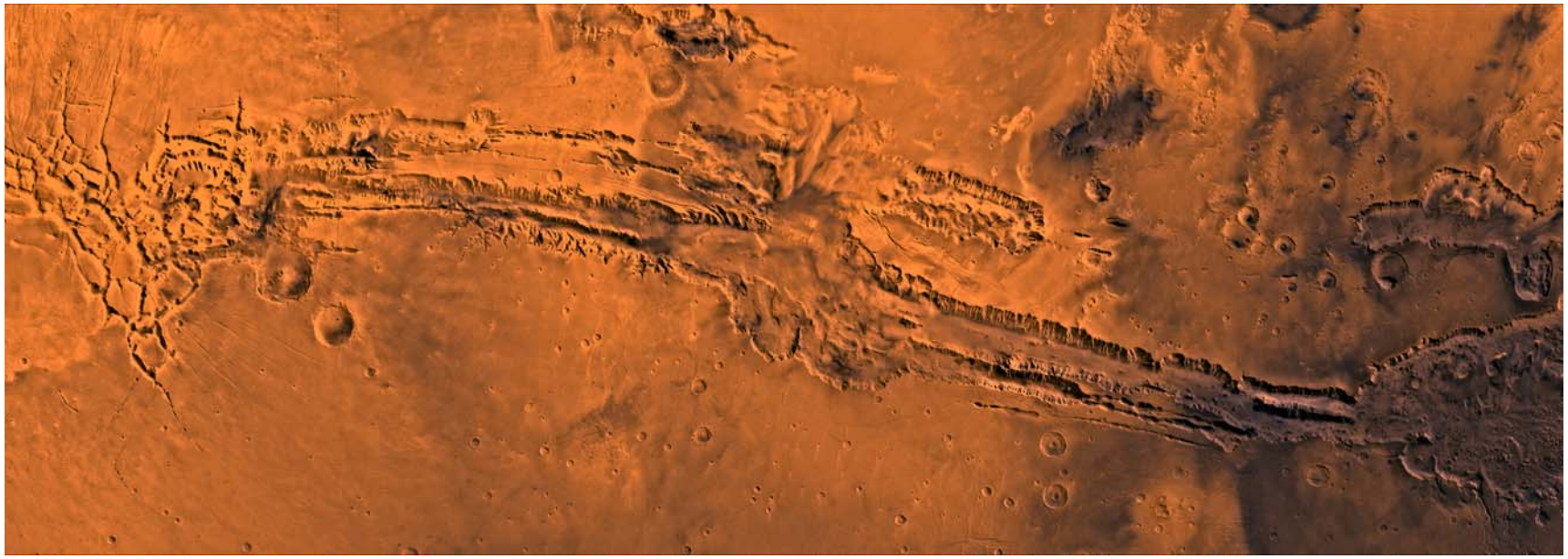

Figure 6-7. A Color Image of Valles Marineris, the Great Canyon of Mars; North Toward Top. The scene shows the entire canyon system, over 3,000 km long and averaging 8 km deep, extending from Noctis Labyrinthus, the arcuate system of grabens to the west, to the chaotic terrain to the east. This image is a composite of Viking medium-resolution images in black and white and low-resolution images in color; Mercator projection. The image extends from latitude 0 degrees to 20 degrees S. and from longitude 45 degrees to 102.5 degrees.

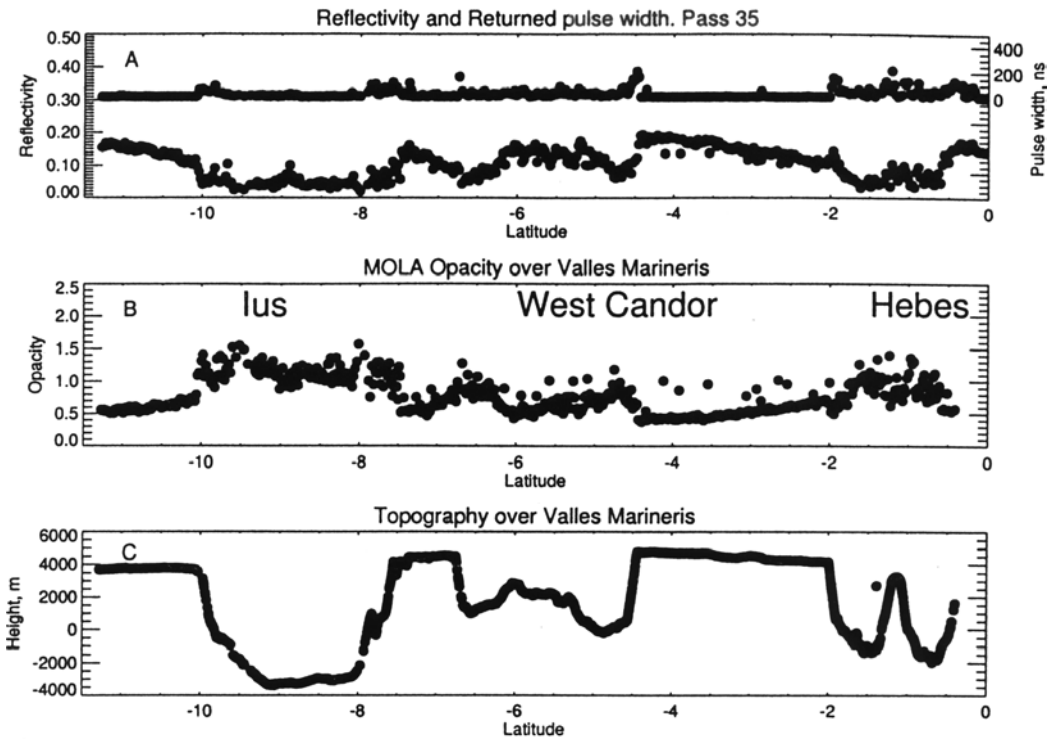

Figure 6-8. Opacity of the Martian Atmosphere Over Valles Marineris Canyon from the Mars Orbiter Laser Altimeter (MOLA) Observations. a) Reflectivity and returned signal pulse width; b) Atmospheric opacity; c) Canyon topography in the latitude range 11° S to 0° N near longitude 77° W [Ivanov and Muhleman, 1998].

Figure 6-9. Artist's Conception of a Mars Airplane Flying over Valles Marineris.

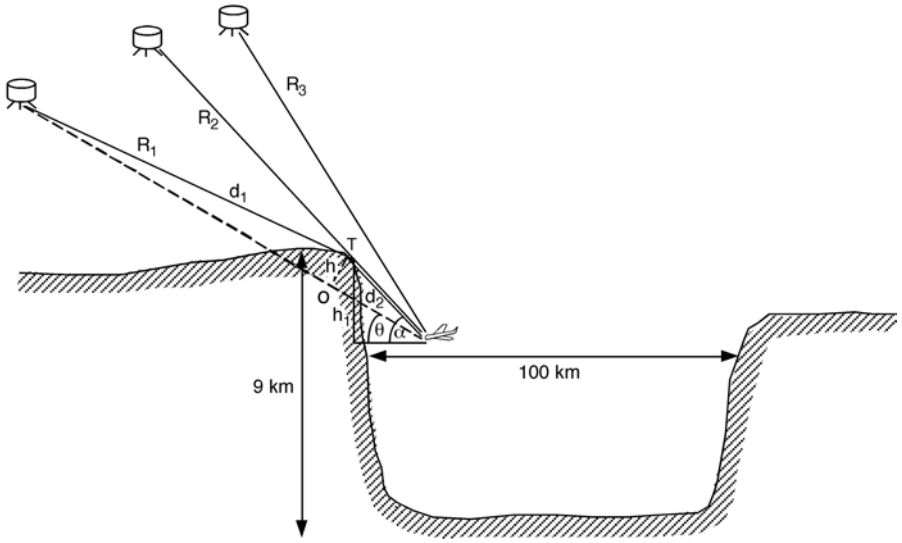

Figure 6-10. Geometric Plot Showing the Ray Paths Between a Satellite and a Mars Airplane. The Mars airplane will fly along a constant atmospheric pressure level. This surface may sometimes be below the canyon edge. However, through refraction and diffraction, the airplane may still maintain communication with satellite.

References

Baker, V.R., et al., Channels and valley networks, in *Mars*, eds. by H.H. Kieffer et al., Univ. of Arizona Press, 493, 1992.

Beckmann, P. and A. Spizzichino, The Scattering of Electromagnetic Waves from Rough Surfaces, New York: Macmillan Co., 1963.

Bedrossian, A., et al., Survey of reflection and scattering measurements of radiowave by Mars surface for communications on and around Mars, *InterPlanetary Network Progress Report*, Jet Propulsion Laboratory, Pasadena, California (in press).

Carr, M.H., *The surface of Mars*, Yale University Press, 1981.

CCIR, Propagation by diffraction, Report 715-2 in Vol. V*, Propagation in Non-ionized Media, Recommendations and Reports of the CCIR*, 1986, Geneva: Int. Telecomm. Union, 1986a.

CCIR, Reflection from the surface of the Earth, Report 1008 in Vol. V*, Propagation in Non-ionized Media, Recommendations and Reports of the CCIR,* 1986, Geneva: Int. Telecomm. Union, 1986b.

Colburn, D., et al., Diurnal variations in optical depth at Mars, *Icarus, 79*, 159, 1989.

Deygout, J., Multiple knife-edge diffraction of microwaves, *IEEE Trans. Veh., Technol. Vol. AP-14,* 480, 1966.

Goldhirsh, J. and W.J. Vogel, *Handbook of Propagation Effects for Vehicular and Personal Mobile Satellite Systems: Overview of Experimental and Modeling Results*, APL-A2A-98-U-0-021, 1998.

Isbell, D., C.M. O'Carroll, and D. Ainsworth, Laser provides first 3-D view of Mars' north pole, Presented at 1998 fall meeting of AGU, San Fracisco, Dec. 6, 1998.

Ivanov, A., and D.O. Muhleman, Opacity of the Martian atmosphere from the Mars Orbiter Laser Altimeter (MOLA) observations, *Geophys. Res. Letts. 25*, 4417, 1998.

Lucchitta, B.K., et al., The canyon system on Mars, in *Mars*, eds. by H.H. Kieffer et al., Univ. of Arizona Press, 453, 1992.

Malin, M.C., and K.S. Edgett, Evidence for recent groundwater seepage and surface runoff on Mars, *Science, 288*, 2330, 2000.

Malin, M.C., et al., Early views of the Martian surface from the Mars Orbiter Camera of Mars Global Surveyor, *Science, 279*, 1681, 1998.

Mouginis-Mark, P.J., et al., The physical volcanology of Mars, in *Mars*, eds. by H.H. Kieffer et al., Univ. of Arizona Press, 424, 1992.

Pollack, J.B., et al., Properties and effects of dust particles suspended in the Martian atmosphere, *J. Geophy. Res., 84*, 2929, 1979.

Simpson, R.A., et al., Radar determination of Mars surface properties, in *Mars*, eds. by H.H. Kieffer et al., Univ. of Arizona Press, 652, 1992.

Smith, D.E., et al., Topography of the northern hemisphere of Mars from the Mars Orbiter Laser Altimeter, *Science, 279*, 1686, 1998.

Thomas, P., et al., Polar deposits of Mars, in *Mars*, eds. by H.H. Kieffer et al., Univ. of Arizona Press, 767, 1992.

Vogel, W.J., and J. Goldhirsh, Fade measurements at L-band and UHF in mountainous terrain for land mobile satellite systems, *IEEE Trans. Anten. Prop., Vol., AP-36*, Jan. 1988.

Wu, S.S.C., Mars synthetic topographic mapping, *Icarus, 33*, 417, 1978.

Zuber, M.T., et al., Observations of the north polar region of Mars from the Mars Orbiter Laser Altimeter, *Science, 282*, 2053, 1998.